Research Article Vol. 34, No. 2 / 26 Jan 2026 / Optics Express 2225
Optics EXPRESS

Time-domain shifting-assisted cepstrum method for complex vibration signal positioning in forward-transmission distributed vibration sensing

GUOQIANG LIU,[1,2] HANJIE LIU,[1,2] XING RAO,[1,2] SHANGWEI DAI,[1,2] LINQIAO DU,[1,2] DANXIA LU,[1,2] RUNLONG ZHU,[1,2] JUNHONG LU,[1,2] MAMOONA KHALID,[3] YIPING WANG,[1,2] AND GEORGE Y. CHEN[1,2,*]

[1]*State Key Laboratory of Radio Frequency Heterogeneous Integration, Key Laboratory of Optoelectronic Devices and Systems of Ministry of Education/Guangdong Province, College of Physics and Optoelectronic Engineering, Shenzhen University, Shenzhen 518060, China*
[2]*Shenzhen Key Laboratory of Ultrafast Laser Micro/Nano Manufacturing, Guangdong and Hong Kong Joint Research Centre for Optical Fibre Sensors, Shenzhen University, Shenzhen 518060, China*
[3]*Photonics and Communications Lab, Electrical Engineering Department, University of Engineering and Technology, Taxila 47050, Pakistan*
[*]*gychen@szu.edu.cn*

Abstract: Aging urban underground pipelines face growing risks, making early damage detection essential. Conventional monitoring methods have limited coverage and scalability. Forward-transmission distributed vibration sensing (FTDVS) can provide real-time condition assessment, but existing positioning methods cannot operate when multiple vibration events overlap in frequency, severely limiting practical application. To address the lack of this critical capability, we propose a time-domain shifting-assisted cepstrum method that extracts primary delays, suppresses dominant components through time-domain shifting, and analyzes residual signals to recover secondary delays. The proof-of-concept experiments results from a 34 km long sensing fiber under three scenarios demonstrate reliable multi-point positioning, achieving positioning accuracies as small as 12.7 m. The results are highly relevant to applications such as real-time pipeline surveillance, security monitoring, and smart city infrastructure assessment.

1. Introduction

The extensive networks of underground pipelines, cables and tunnels form the hidden backbone of urban infrastructure [1]. However, these systems are increasingly vulnerable to damage from aging, nearby construction activities, and even malicious sabotage [2]. Timely detection of these activities is essential to mitigating service disruptions and structural failures [3]. Conventional inspection techniques are constrained by limited spatial coverage, delayed response time, and substantial operational cost, rendering them inadequate for real-time, large-scale monitoring [4]. Distributed vibration sensing (DVS) using optical fiber has emerged as a promising class of technologies that offers distinct advantages over traditional electrical sensors, including long sensing range, high sensitivity, immunity to electromagnetic interference, and robustness in harsh environments [5]. These characteristics of fiber-optic DVS present a particularly attractive solution for scalable, real-time monitoring of underground infrastructure.

DVS technologies can be broadly categorized into two types: backscatter-based and forward-transmission-based systems (FTDVS) [6]. Backscatter-based DVS systems, such as optical time-domain reflectometry (OTDR) and optical frequency-domain reflectometry (OFDR), utilize Rayleigh backscattered light as the sensing mechanism for detecting localized perturbations

#580991 https://doi.org/10.1364/OE.580991
Journal © 2026 Received 7 Oct 2025; revised 11 Dec 2025; accepted 12 Dec 2025; published 16 Jan 2026

Optics EXPRESS

[7–9]. By employing interferometric configurations such as Sagnac interferometers (SI) or Mach–Zehnder interferometers (MZI), FTDVS extracts phase information from interference signals for vibration monitoring and positioning [10–14]. Since the forward-propagating signal is several orders of magnitude stronger than its backscattered light, FTDVS offers a significantly better signal-to-noise ratio compared to their backscatter-based counterparts [15]. Moreover, optical fibers are already extensively deployed in urban environments for communication purposes [16], such as underneath building flooring or under pavements. If forward-transmission sensing can be integrated into existing communication systems [17], the fiber networks upgrade to dual-purpose as a scalable and low-cost platform for continuous underground infrastructure monitoring – particularly in pipeline systems where high spatial coverage and low latency are required. Recent progress has also demonstrated that forward-transmission systems can detect weak real-world vibration events under strong environmental noise through adaptive time-frequency masking, further highlighting the potential of this sensing architecture [18]. Such T–F–masking-based approaches provide excellent sensitivity and noise suppression for detecting and localizing weak real-world events, but they are primarily designed for one dominant event at a time rather than simultaneous localization of multiple fully overlapped vibration sources. In practical deployments, vibration activities along long fibers are generally sparse, however, two independent disturbances—such as construction impacts overlapping with traffic or human-induced vibrations—may still coincide within the same short analysis window and therefore require reliable separation. In contrast, the probability of three or more independent broadband events occurring simultaneously is extremely low. Even under these practical conditions, most FTDVS methods encounter significant challenges when multiple vibration events occur simultaneously [19]. In particular, existing multi-event localization schemes each exhibit clear strengths but are usually built on simplifying assumptions such as identical spectral content between vibration sources or single-frequency excitations at distinct frequencies, which limits their applicability to broadband events distributed along the fiber [20–23]. Among these works, ultra-long forward-transmission schemes demonstrate thousand-kilometer–scale sensing with a wide frequency response, and dual-sensor adaptive beamforming techniques provide strong interference rejection through coherent multi-receiver processing; however, these approaches are essentially tailored to single-event or partially separated sources and therefore cannot rigorously resolve fully overlapped broadband events. Recent work using mirror-image correlation can localize multiple events with overlapping time traces by exploiting contrasts between their transient and stationary stages. However, since it depends on distinguishable transients and requires iterative delay scanning, its performance degrades when broadband transients fully coincide, makes it less suitable for fully superimposed broadband events and real-time operation [24]. Beyond interferometric signal processing, multi-event localization has also been explored using deep-learning models in Sagnac-based systems. Such data-driven approaches can achieve highly accurate multi-point localization after training by regressing vibration positions from learned spectral patterns, yet they rely heavily on supervised training and often require scenario-specific retraining, which limits their convenience and generalizability to arbitrary broadband vibration signatures [25]. This limitation reduces the practicality of FTDVS in complex urban settings, where diverse and overlapping vibration sources are prevalent.

In this work, we address a critical gap in FTDVS and present a new positioning method for complex vibration signals (broadband and overlapping). A dual Mach-Zehnder interferometric system is employed for extracting optical phase variations, integrated with a cepstrum and time-domain shifting method to estimate both relative and absolute delays of overlapping vibration signals [26]. This framework extends cepstrum-based delay estimation beyond single-source or identical-source conditions, enabling accurate localization of overlapping broadband vibrations with distinct spectral characteristics.

Optics EXPRESS

2. Principle and methodology

In the proposed forward-transmission distributed vibration sensing (FTDVS) system, two optical beams of identical wavelength are launched in opposite directions through a common single-mode fiber. External vibrations acting on the fiber induce axial strain and variation in the effective index, which in turn modulate the phase delay of light. These phase-modulated signals are subsequently extracted at the photodetector pairs. When multiple segments along the sensing fiber are simultaneously subjected to different vibrations, the phase signals detected at each end of the fiber represent a superposition of vibration components with different time delays, as illustrated in Fig. 1.

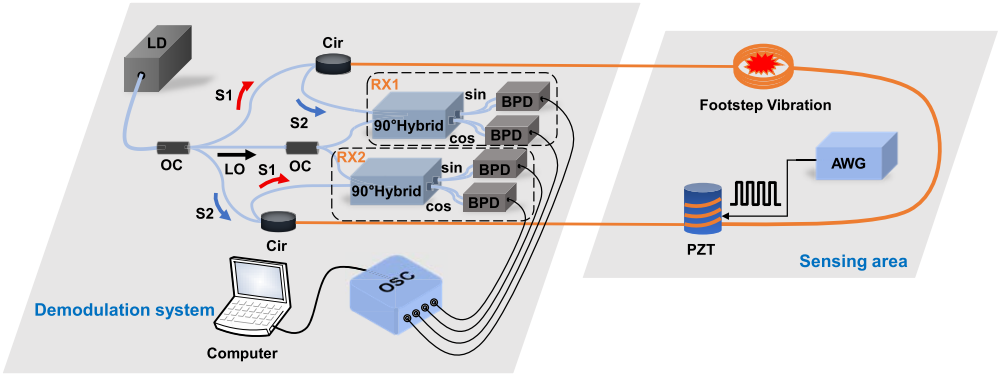

Fig. 1. Forward-transmission distributed sensing system based on a dual Mach–Zehnder interferometer. LD: laser diode; OC: optical coupler; S1, S2: signal light; LO: local light; Cir: circulator; RX: receiver; AWG: arbitrary waveform generator; PZT: piezoelectric transducer; BPD: balanced photodetector; OSC: oscilloscope.

The optical signals from path S1 and path S2 can be expressed as:

$$E_1 = \sqrt{P}\cos(\omega t + \varphi_{n1}(t) + \varphi_{v1}(t - \tau_{1,1}) + \varphi_{v2}(t - \tau_{2,1})) \tag{1}$$

$$E_2 = \sqrt{P}\cos(\omega t + \varphi_{n2}(t) + \varphi_{v1}(t - \tau_{1,2}) + \varphi_{v2}(t - \tau_{2,2})) \tag{2}$$

The local signal can be expressed as:

$$E_{LO} = \sqrt{P}\cos(\omega t) \tag{3}$$

Here, P denotes the signal power and ω is the angular frequency. $\varphi_{n1}(t)$ and $\varphi_{n2}(t)$ denote independent phase noise contributions originating from the photodetection and electronic circuitry, including shot noise, thermal noise, amplifier noise, and residual imbalance. $\varphi_{vi}(t)$ denotes the phase modulation caused by vibration source i. The propagation times from vibration source i to RX1 and RX2 are denoted by $\tau_{i,1}$ and $\tau_{i,2}$, respectively.

The relative propagation delay of vibration source i between RX1 and RX2 can be expressed as:

$$\Delta t_i = \tau_{i,2} - \tau_{i,1} \tag{4}$$

The demodulated phases of the path 1 and path 2 signals can be expressed as [27]:

$$\varphi_1(t) = \varphi_{n1}(t) + \varphi_{v1}(t - \tau_{1,1}) + \varphi_{v2}(t - \tau_{2,1}) \tag{5}$$

$$\varphi_2(t) = \varphi_{n2}(t) + \varphi_{v1}(t - \tau_{1,2}) + \varphi_{v2}(t - \tau_{2,2}) \tag{6}$$

Optics EXPRESS

By subtracting the two signals, the resulting expression can be reformulated in a convolutional form:

$$\begin{aligned}\varphi(t) = \varphi_1(t) - \varphi_2(t) &= \varphi_n(t) + \sum_{i=1}^{2} \varphi_{vi}(t - \tau_{i,1}) * (\delta(t) - \delta(t - \Delta t_i)) \\ &= \varphi_n(t) + \sum_{i=1}^{2} \varphi_{vi}(t - \tau_{i,1}) * h_i(t)\end{aligned} \tag{7}$$

where $\varphi_n(t) = \varphi_{n1}(t) - \varphi_{n2}(t)$ and $h_i(t) = \delta(t) - \delta(t - \Delta t_i)$. $\varphi_n(t)$ represents the residual noise after subtracting the independent photodetection and electronic noise contributions from the two receiving paths, $\delta(t)$ denotes the Dirac delta function and $h_i(t)$ represents the difference between the impulse responses of the two signal paths corresponding to vibration source i, with RX1 taken as the reference point.

Let $\Psi_n(f)$, $\Psi_{vi}(f)$ and $H_i(f)$ denote the Fourier transforms of signals $\varphi_n(t)$, $\varphi_{vi}(t - \tau_{i,1})$ and $h_i(t)$, respectively. The Fourier transform of the Eq. (7) can be expressed as:

$$\Psi(f) = \mathcal{F}\{\varphi(t)\} = \Psi_n(f) + \sum_{i=1}^{2} \Psi_{vi}(f) H_i(f) \tag{8}$$

The corresponding time delays Δt_i can then be determined from $H_i(f)$ and the magnitude of $H_i(f)$ typically exhibits a sine-like envelope of the form:

$$|H_i(f)| = |1 - e^{-i2\pi f \Delta t_i}| = 2 \sin |\pi f \Delta t_i| \tag{9}$$

By taking the logarithm of the magnitude spectrum of $\Psi(f)$ and then applying the inverse Fourier transform for $i, j \in \{1, 2\}, i \neq j$, the resulting signal of Eq. (8) can be approximated as (see Appendix A for derivation):

$$C_\varphi(\tau) = \mathcal{F}^{-1}\{\log |\Psi(f)|\} \approx -\sum_{m \neq 0} A_m \delta(\tau - m|\Delta t_1|) - \sum_{n \neq 0} B_n \delta(\tau - n|\Delta t_2|) + C_{base}(\tau) \tag{10}$$

A_m and B_n in Eq. (10) denote the amplitude of the m-th and n-th peaks, respectively. The impulses $\delta(\tau - m|\Delta t_1|)$ and $\delta(\tau - n|\Delta t_2|)$ therefore yield waveform peaks at $\tau = m|\Delta t_1|$ and $\tau = n|\Delta t_2|$, respectively. However, in practice, the baseline term $C_{base}(\tau)$ arising from the broadband envelope and residual coupling, produces a smooth background signal that tends to obscure weaker peaks, such that only the fundamental peak remains clearly observable in the cepstrum.

It should be noted that Eq. (10) provides only the magnitude of the relative delay (i.e. $\tau = |\Delta t_1|$), while the sign of the delay remains indeterminate due to the inherent symmetry of the forward-transmission geometry. To resolve this ambiguity, the energy of the residual signal in the time domain is analyzed. The detailed derivation and justification of this sign determination method are provided in Appendix B.

For the subsequent analysis, it is assumed that the identified delay corresponds to a positive value $\Delta t_1 > 0$. Based on the estimated delay Δt_1, a time delay function $\delta(t - \Delta t_1)$ is constructed and convolved with $\varphi_1(t)$ to implement the time-domain shifting operation. Subtracting $\varphi_2(t)$ from the shifted signal yields the residual signal that can be expressed as:

$$\begin{aligned}S(t) &= \varphi_1(t) * \delta(t - \Delta t_1) - \varphi_2(t) \\ &= \varphi_{n1}(t - \Delta t_1) - \varphi_{n2}(t) + \varphi_{v2}(t - \tau_{2,1}) * [\delta(t) - \delta(t - \Delta t_2 + \Delta t_1)] \\ &= \varphi_n(t) - \varphi_{n1}(t) * [\delta(t) - \delta(t - \Delta t_1)] + \varphi_{v2}(t - \tau_{2,1}) * [\delta(t) - \delta(t - \Delta t_2 + \Delta t_1)]\end{aligned} \tag{11}$$

Although the acquired signal exhibits a long temporal duration, the majority consisted of noise and baseline fluctuations, which could distort the cepstrum analysis. To mitigate these effects,

Optics EXPRESS

only the desired portion of the signal was retained by identifying the point of maximum absolute amplitude and applying a symmetric time window centered around it, while the remaining segments were replaced with a constant value to ensure stability in subsequent processing. By applying the cepstrum method to the nominal portion of Eq. (11), and following the derivation steps detailed in Appendix A, the resulting signal can be approximated as:

$$\begin{aligned} C_S(\tau) &= \mathcal{F}^{-1}\{\log\{|\mathcal{F}(S(t))|\}\} \\ &\approx -\sum_{m\neq 0} A_m \delta(\tau - m(|\Delta t_2 - \Delta t_1|)) - \sum_{n\neq 0} B_n \delta(\tau - n|\Delta t_1|) + C_{base}(\tau) \end{aligned} \tag{12}$$

The time delay $|\Delta t_2 - \Delta t_1|$ can be extracted from the peak position. Consequently, the second time delay Δt_2 is determined by combining this value with previous estimated time delay Δt_1(see Appendix B for the detailed derivation). These delay estimates are substituted into the position estimation model to calculate the vibration position. The position of i-th vibration source, x_i, can be expressed as:

$$x_i = \frac{1}{2}\left(L - c\frac{\Delta t_i}{n}\right) \tag{13}$$

where L in Eq. (13) is the length of the sensing fiber, $c = 299{,}792{,}458$ m/s, is the speed of light in vacuum, and n is the effective index of the fiber. In the discrete-time implementation with sampling rate f_s, the minimum resolvable delay is one sample $\Delta t_{min} = 1/f_s$. By substituting Δt_{min} into the position model, the nominal spatial resolution can be obtained:

$$\Delta x = \frac{c}{2nf_s} \tag{14}$$

The overall procedure for locating two vibration sources is illustrated in the flow chart shown in Fig. 2.

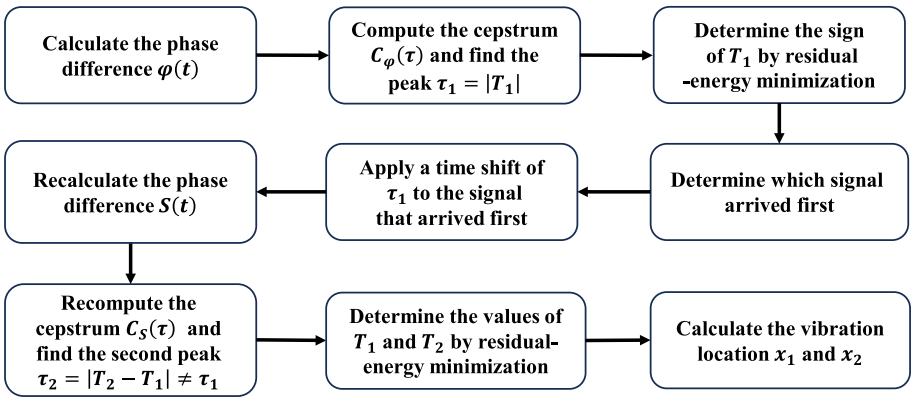

Fig. 2. Flow chart of the proposed cepstrum-based vibration localization method.

3. Experimental setup

In the multi-point complex vibration experiment, the laser source used was an NKT Photonics E15 narrow-linewidth laser (100 Hz linewidth), operating at a central wavelength of 1550 nm with an output power of 20 mW. The laser output was divided by a 3×3 coupler into two signal paths (S1 and S2) and one local oscillator (LO) reference path. The LO path was subsequently

Optics EXPRESS

split by a 50:50 coupler into two beams of equal optical intensity, which served as reference signals for interference.

The sensing fiber used is a standard single-mode fiber (SSMF, ITU-T G.652.D) with an effective index of $n = 1.467$ and length of 34 km. Vibrations are induced on the fiber through either piezoelectric transducer (PZT)s, footstep or knocking. The total fiber length (34 km) and the positions of the vibration sources (9.74 km and 13.87 km) were determined using a commercial OTDR. The PZT exhibits a responsivity of 452.31 rad/V for the 52.32-m fiber segment and was driven by an arbitrary waveform generator (AWG).

The signal light in paths S1 and S2 propagated along different routes through the sensing fiber, undergoing distinct phase modulations induced by the respective external vibrations. The modulated signals were directed through circulators 1 and 2 and subsequently coherently combined with the two reference beams in a 90° optical hybrid. The interference outputs were detected by a balanced photodetector (BPD) with a 100 MHz bandwidth, converted into electrical signals, and digitized using an oscilloscope operating with a sampling rate of 10 MHz for subsequent signal processing.

4. Experimental results and discussion

To comprehensively assess the performance of the proposed method, three representative categories of vibration signals were investigated: (i) periodic square waves with varying duty cycles generated by PZTs, (ii) a footstep applied to the fiber laid directly on the ground, and (iii) a knocking event on the fiber. Figure 3 presents the corresponding time-domain phase responses for these cases. The square-wave excitations, shown in Figs. 3(a) and 3(b), led to distinct, periodic phase shifts associated with the rising and falling edges of the pulses. In contrast, the random excitation events, as illustrated in Figs. 3(c) and 3(d), yield irregular fluctuating patterns. The footstep response is characterized by an abrupt phase decrease followed by gradual recovery, whereas the knocking event produces oscillatory variations without strict periodicity.

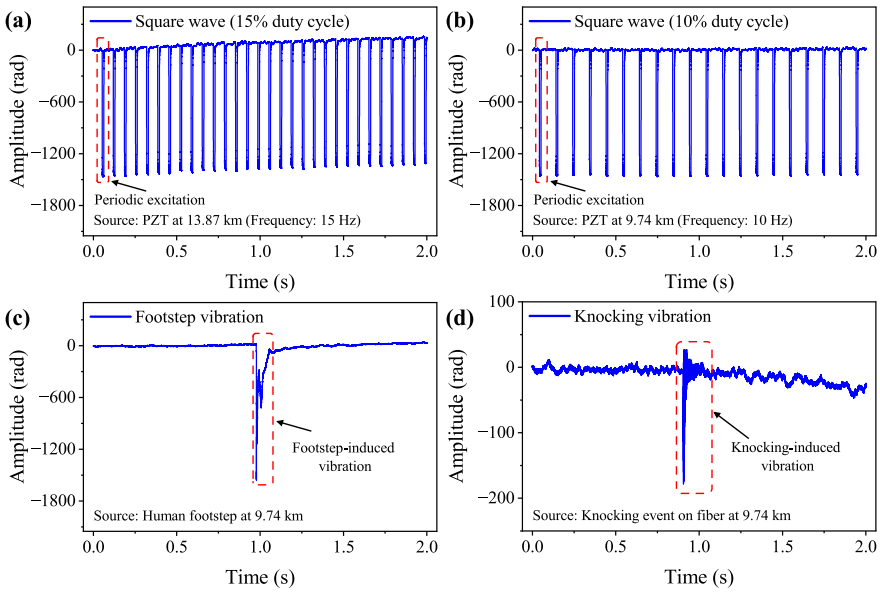

Fig. 3. Time-domain phase response of four representative vibration signals: (a) Square wave with 15% duty cycle; (b) Square wave with 10% duty cycle; (c) Footstep-induced vibration; (d) Knocking-induced vibration.

Optics EXPRESS

The corresponding frequency-domain spectra are presented in Fig. 4. The square waves in Figs. 4(a) and 4(b) exhibit harmonic components at integer multiples of the excitation frequency, with higher-order components attenuating with increasing frequency. The footstep response in Fig. 4(c) concentrated its energy at the lower frequencies, reflecting the slow and transient nature of the disturbance. By contrast, the knocking response in Fig. 4(d) shows oscillatory spectral features with multiple low-frequency peaks. Despite these differences in the low-frequency region, all four signal types exhibit a similar spectral trend in the mid-to-high-frequency range, where the energy decays uniformly with increasing frequency.

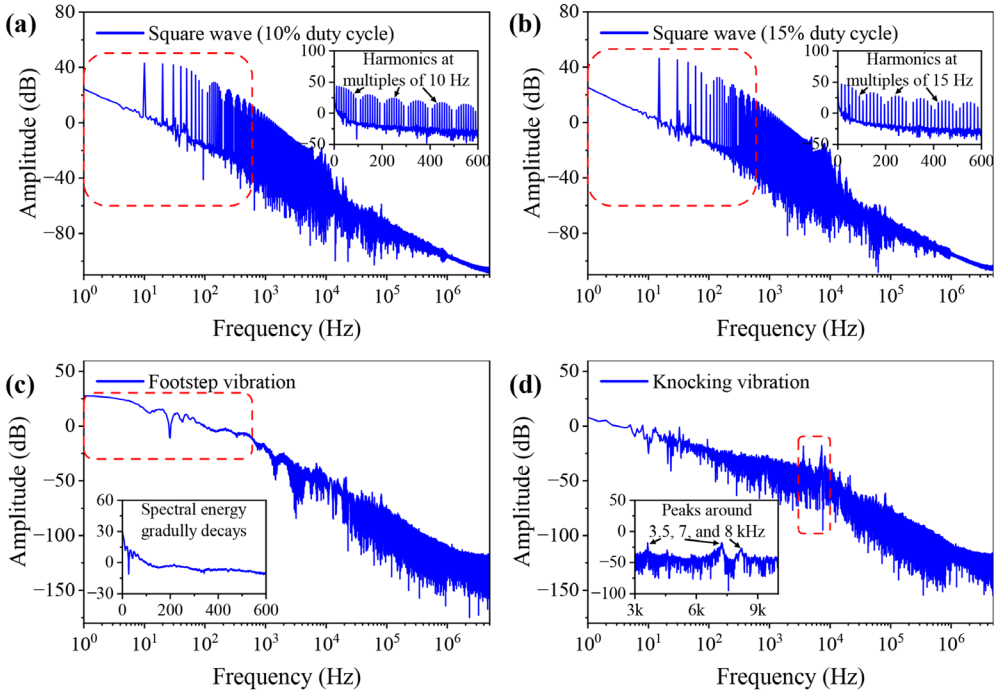

Fig. 4. Frequency-domain spectra of four vibration signals: (a) Square wave (15% duty cycle, harmonics at 15 Hz multiples); (b) Square wave (10% duty cycle, harmonics at 10 Hz multiples); (c) Footstep vibration with energy gradually decaying beyond a few hundred hertz; (d) Knocking vibration with a dominant peak around 3.5, 7 and 8 kHz. All signals show uniformly decaying spectral energy in the mid-to-high-frequency range, consistent with broadband characteristics.

In the multi-point vibration experiment, a piezoelectric transducer (PZT) was placed at the 13.87 km position of the sensing fiber. A periodic pulse excitation with an amplitude of 2 V, frequency of 15 Hz, and a duty cycle of 15% was applied through the AWG to facilitate controllable vibrations. Meanwhile, at the 9.74 km position, the fiber was laid directly on the ground, and pedestrian walking was simulated by stepping on the fiber. The experimental results are shown in Figs. 5 and 6. Figure 5 illustrates the localization of the first vibration source using the proposed cepstrum-based method. In Fig. 5(a), the two demodulated phase signals are shown, where both vibrations occur simultaneously within the same time window. The differential phase signal, $\varphi(t) = \varphi_1(t) - \varphi_2(t)$, is plotted in Fig. 5(b), with its corresponding spectrum displayed in Fig. 5(c). In the spectrum, the low-frequency region is dominated by the square-wave excitation, while the periodic spacing $\Delta f_1 = \frac{1}{\tau_1}$ arises from the envelope modulation imposed by the time delay. The cepstrum of $\varphi(t)$ is given in Fig. 5(d), where the true minimum is identified using a detection threshold derived from the baseline noise floor combined with the

Optics EXPRESS

standard deviation of the lower-envelope fluctuations, revealing a relative time-delay difference of 30.5 μs corresponding to one of the vibration sources, while the second source will be resolved at the next stage.

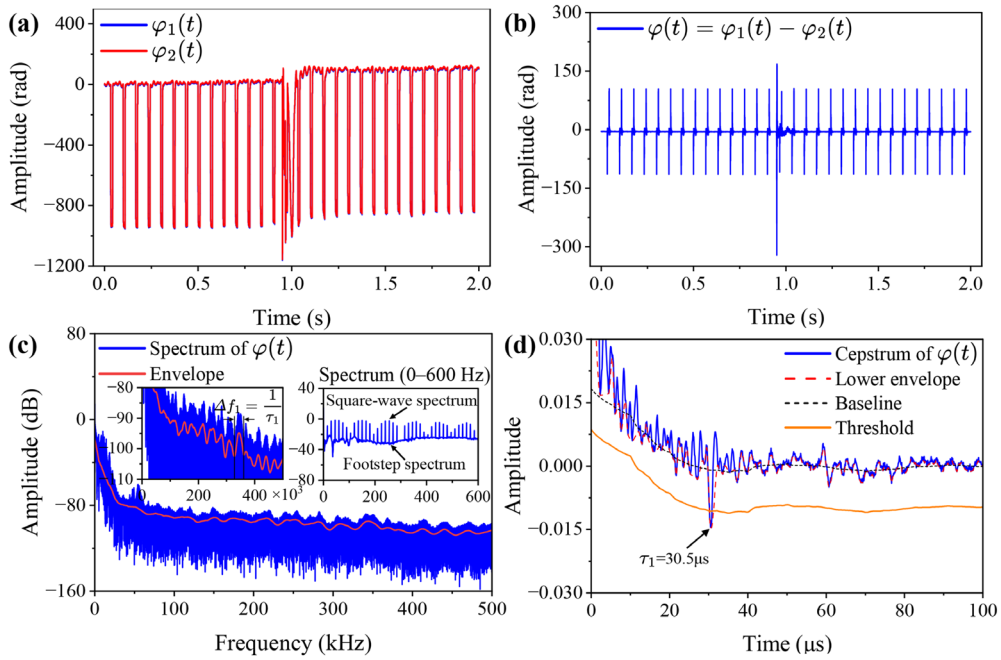

Fig. 5. Location of the first vibration source using the proposed cepstrum-based method: (a) Demodulated phase signals $\varphi_1(t)$ and $\varphi_2(t)$; (b) Differential phase signal $\varphi(t)$; (c) Spectrum of the differential signal from (b); (d) Cepstrum result of $\varphi(t)$, showing the first time delay difference of 30.5 μs.

The localization of the second vibration source using the cepstrum-based method is illustrated in Fig. 6. To extract the second vibration, $\varphi_1(t)$ was shifted by 30.5 μs in the time domain and then subtract $\varphi_2(t)$ as shown in Fig. 6(a). To focus the analysis on the weaker event rather than on baseline fluctuations, the residual signal in Fig. 6(a) is first examined to identify the peak of the localized disturbance. A symmetric 0.02-s truncation window (±0.01 s around the peak) is then applied to crop the neighborhood of this event, and the remaining portions of the waveform are replaced with a constant value to stabilize the subsequent spectrum and cepstrum calculations. An additional subfigure displays this cropped/truncated segment, highlighting that the dominant vibration is largely suppressed after time-domain alignment, while the weaker vibration becomes clearly visible. The 0.02-s duration is chosen because it covers the temporal region where the weaker vibration carries most of its energy, ensuring that the truncated signal preserves the signal of the second event while excluding unrelated baseline variations. The use of a time window in this stage is not intrinsic to the proposed algorithm, but is required only because the second vibration is a short-duration event: after cancellation of the dominant source, the residual signal $S(t)$ exhibits a localized peak associated with the weaker event; a symmetric window centered on this peak (e.g., ±0.01 s in the experiments) is used to capture most of its energy while excluding noise-only regions. For the first cepstrum stage, no additional windowing is necessary in our experiments because the square-wave excitation persists throughout the entire 2-s recording, and both vibration events span the full measurement duration. Thus, the whole record naturally serves as the analysis window and already contains the complete fringe contributions from both delays. This simple energy-based, non-iterative rule adapts the window length to the actual duration of

Optics EXPRESS

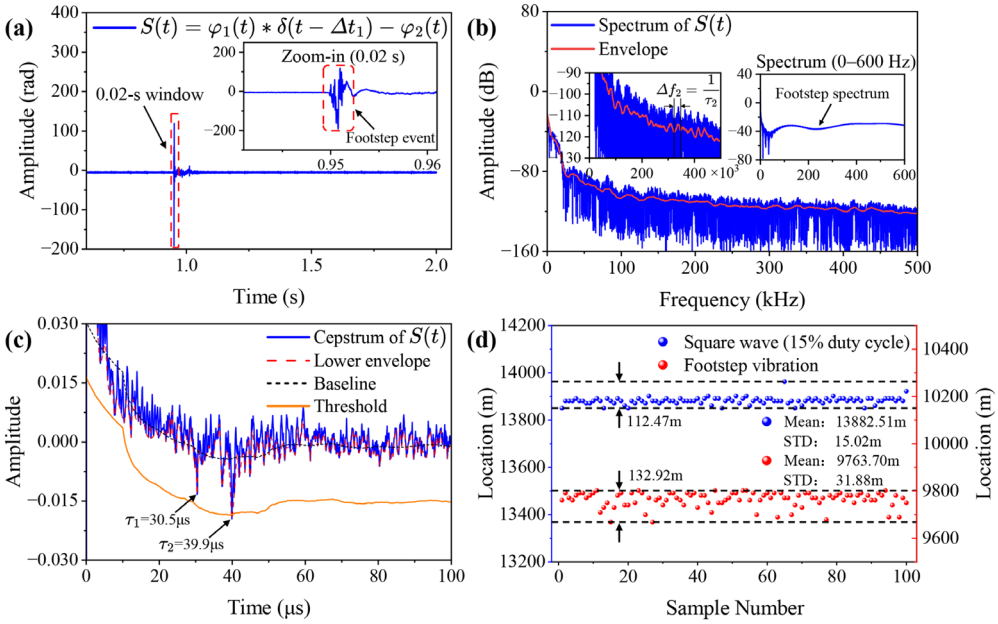

Fig. 6. Location of the second vibration source using proposed cepstrum-based method: (a) Residual phase signal $S(t)$ is obtained by first shifting $\varphi_1(t)$ by 30.5 μs then subtracting $\varphi_2(t)$, an inset shows the cropped/truncated 0.02-s segment used for the second-stage cepstrum analysis; (b) Spectrum of the residual signal from (a); (c) Cepstrum result of the residual signal in (a), revealing an additional relative time delay difference of 39.9 μs; (d) Positioning accuracy for the vibration sources.

the vibration and enhances the signal-to-noise ratio (SNR) of the weaker event. In the spectrum of the truncated $S(t)$, the delay-subtraction operation suppresses the square-wave-induced fringes from the first vibration source, while the weaker footstep vibration produces a clear envelope modulation whose fringe spacing becomes more pronounced, as shown in the inset of Fig. 6(b). The delay corresponding to the second vibration is identified using a threshold determined from the baseline noise floor together with the standard deviation of the lower-envelope fluctuations, ensuring that the true delay can be reliably distinguished. The corresponding cepstrum in Fig. 6(c) reveals an additional relative time delay difference of 39.9 μs. Combining this value with the previously identified delay yields an absolute time delay of 70.4 μs for the second vibration source. Substituting these delays into Eq. (13), provides vibration positions of 13,881.39 m and 9,801.64 m. After 100 successive experiments, the estimated mean positions were 13,882.51 m and 9,763.70 m, with standard deviations (positioning accuracy) of 15.02 m and 31.88 m, and maximum position errors of 112.47 m and 132.92 m, respectively, as summarized in Fig. 6(d). The findings validate the capability of the proposed method to reliably distinguish and localize simultaneous multi-point vibrations along the sensing fiber.

Building on the results of Figs. 5 and 6, where two simultaneous events were successfully localized, additional experiments were conducted to evaluate the positioning accuracy of the proposed method under all four different vibration types. Two groups of two-point vibration experiments were performed, with the actual vibration positions fixed at 13.87 km and 9.74 km along the sensing fiber. The corresponding localization results are summarized in Fig. 7.

In the first case, two square-wave excitations with duty cycles of 15% and 10% were simultaneously applied. The estimated mean positions were 13,895.40 m and 9,744.07 m, with corresponding standard deviations of 12.72 m and 22.92 m, and maximum errors of 71.57 m

Optics EXPRESS

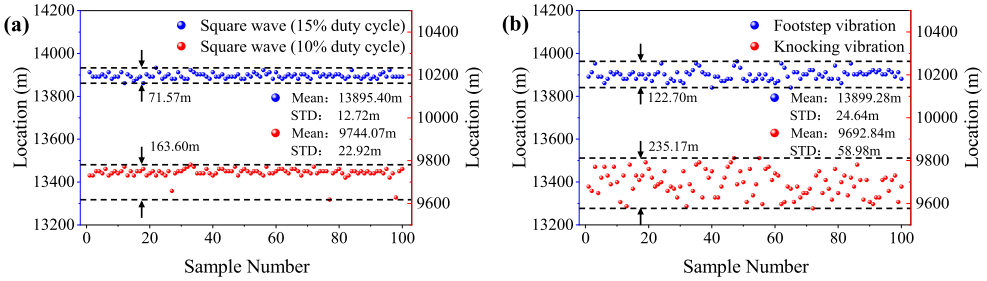

Fig. 7. Positioning accuracy of the proposed method for different vibration signals at 13.87 km and 9.74 km: (a) Two square-wave excitations with different duty cycles (15% and 10%); and (b) Footstep and knocking vibrations.

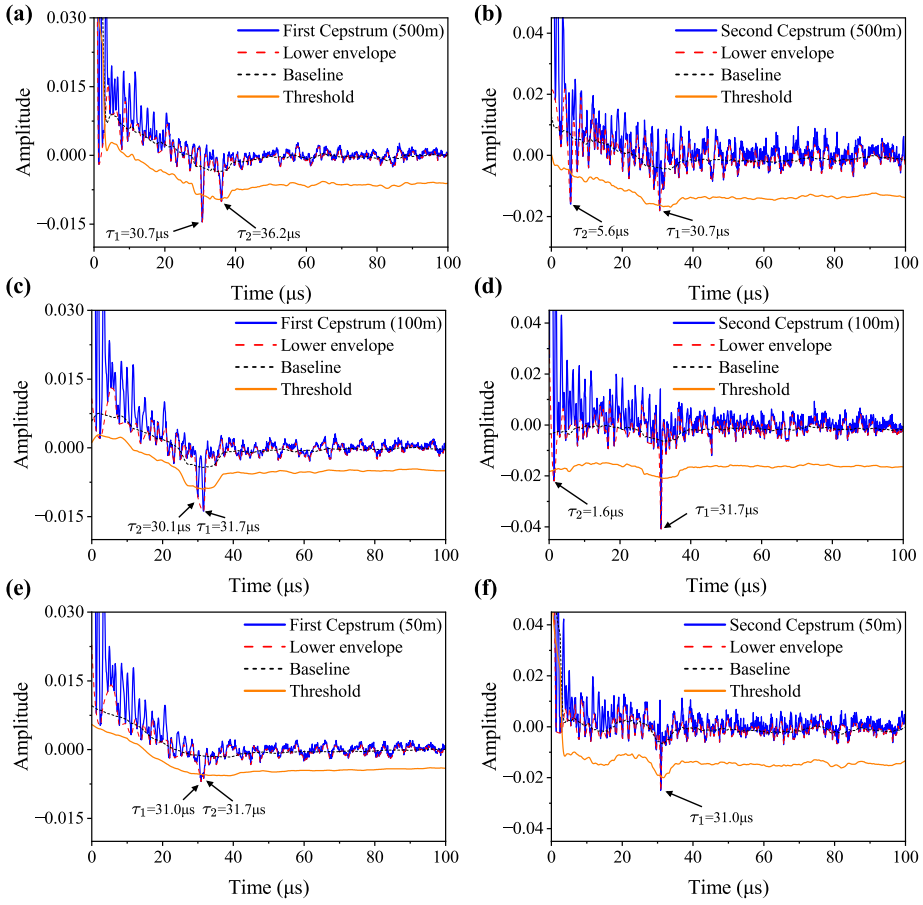

Fig. 8. Cepstrum results for two comparable-strength vibration sources: (a–b) Large spacing (500 m): two peaks remain clearly resolvable in both the first and second cepstrum; (c–d) Moderate spacing (100 m): two peaks are still resolvable, but in the second cepstrum, the weaker peak lies closer to zero delay and partially overlaps with the intrinsic baseline, which reduces its visibility; and (e–f) Small spacing (50 m): in the first cepstrum, the two delay peaks merge into one broadened peak, while in the second cepstrum, the shifted peak moves very close to zero delay and is almost completely buried by the baseline.

Optics EXPRESS

and 163.60 m. In the second case, a footstep vibration and a knocking vibration were imposed simultaneously. The estimated mean positions were 13,899.28 m and 9,692.84 m, with standard deviations of 24.64 m and 58.98 m, and maximum errors of 122.70 m and 235.17 m, respectively. These results demonstrate that the proposed method can viably locate two simultaneous vibrations along the sensing fiber. Although larger deviations were observed for irregular impulsive signals such as knocking, the method consistently provided reliable localization across different vibration types.

To further evaluate the practical separability of dual vibration events with comparable strength, additional experiments were conducted using two square-wave excitations (15 Hz, 15% duty and 10 Hz, 10% duty). Since the cepstrum peak reflects the differential propagation delay, only the relative spacing between the two vibration points is considered in this experiment. The spacing was varied from 500 m to 50 m, and the corresponding first and second cepstrum results are shown in Fig. 8.

When the spacing was 500 m, two distinct delay peaks were clearly observed in both the first and second cepstrum results, confirming that the proposed method can reliably separate two comparable-strength vibration events when the delay difference is sufficiently large. When the spacing was reduced to 100 m, the two peaks remained resolvable. However, in the second cepstrum the weaker peak was shifted closer to zero delay, where partial overlap with the baseline occurs, leading to reduced peak visibility compared with the first cepstrum. For the 50 m case, the two delay peaks almost completely overlapped in the first cepstrum, forming a single broadened peak. In the second cepstrum, the shifted peak moved even closer to zero delay and became nearly buried in the baseline, making the two events indistinguishable. In this case, the effective delay becomes too small for the available vibration bandwidth to support the required spectral modulation, making the two events indistinguishable. These observations indicate that the practical separability of two comparable-strength vibration sources is on the order of 50–100 m, owing to intrinsic cepstrum peak overlap near zero delay and the insufficient vibration bandwidth to sustain the required spectral modulation when the residual delay becomes extremely small. It should be stressed that even when two peaks are visible in the first cepstrum for comparable-strength events, this step only provides the absolute delays of the two vibrations. With the second cepstrum, the sign relationship between these delays can be identified, enabling the two vibration positions to be uniquely determined.

Although the proposed forward-transmission distributed vibration sensing method demonstrates the feasibility of localizing simultaneous two-point vibrations of different characteristics, several limitations remain. As shown in Fig. 8, the ability to resolve two comparable-strength vibration sources is primarily constrained by the intrinsic overlap of their cepstrum peaks and by the baseline behavior near zero delay. As a result, the practical separability between two simultaneous vibration events is on the order of 50–100 m, whereas the theoretical delay resolution of 10.22 m applies to a single vibration event. Aside from the separability limitation, the method is further affected by several intrinsic factors. First, the cepstrum-based approach assumes that the vibration signals are broadband and spectrally uniform. In practice, the slowly varying components of vibration signals often deviate from this assumption, giving rise to residual peaks that can obscure the true delay features. Consequently, the estimated delay differences might not always be distinct, and the corresponding cepstral peaks may lack sufficient prominence. Second, the method relies on dual demodulation channels, which inherently limits its capacity to resolve more than two simultaneous vibrations. When three or more vibration sources coexist, the linear combination of two demodulated signals can, at best, cancel a single component, leaving the remaining signals entangled. Under these conditions, the time-domain shifting strategy cannot fully isolate all differential signals, and weaker cepstral peaks may be severely masked. Overcoming these limitations may require the adoption of advanced multi-channel demodulation, blind source separation method, or machine learning-based approaches.

Optics EXPRESS

5. Conclusion

In this work, we proposed and experimentally validated a new positioning method for forward-transmission DVS of complex vibration signals (broadband and overlapping). The core algorithm integrates time-domain shifting with cepstrum analysis, which enables separation and accurate on-fiber positioning of two overlapping broadband vibration signal events along a 34 km long sensing fiber. The experimental results demonstrated a nominal spatial resolution of 10.22 m with a 10 MHz sampling rate, along with positioning accuracies (standard deviations) ranging from 12.72 m to 58.98 m under diverse vibration scenarios, including square-wave excitations, footsteps and knocking events. For comparable-strength events, the practical separability between two vibration points is approximately 50–100 m.

These findings confirm the reliability of the proposed method for two-point vibration positioning. Beyond validating its feasibility, this study advances cepstrum-based delay estimation from traditional single-source and identical-signal cases to complex scenarios involving overlapping broadband vibrations. By extending the applicability of forward-transmission DVS to more realistic multi-signal environments, the method addresses a critical gap in current positioning techniques. Although the present framework does not yet generalize to situations involving more than two simultaneous vibration sources, it provides a strong basis for methodological refinements, such as multi-channel demodulation, blind source separation, and machine learning-assisted signal processing. This demonstrates a clear pathway toward scalable sensing strategies that can enhance the long-term reliability of critical infrastructure.

Appendix A: Derivation of the time delay estimation

This appendix provides the detailed derivation of the delay estimation formula (Eqs. (8)–(10)) based on the cepstrum of $\varphi(t)$. Starting from Eq. (8).

For $i \neq j$, $\Psi(f)$ can be expressed as:

$$\Psi(f) = \Psi_{vi}(f)[H_i(f) + r(f)], r(f) = \frac{\Psi_n(f) + \Psi_{vj}(f)H_j(f)}{\Psi_{vi}(f)} \tag{15}$$

Let $f_k = k/\Delta t_i$ denote the k-th zero of $H_i(f)$. We introduce the notation:

$$\delta = f - f_k, \alpha = 2\pi\Delta t_i \tag{16}$$

In the neighborhood $\delta \ll 1/\alpha$, we have:

$$H_i(f) = 1 - e^{-i2\pi(f_k+\delta)\Delta t_i} = 1 - e^{-i2\pi\delta\Delta t_i} \approx i\alpha\delta \tag{17}$$

Since the spectrum $\Psi_{vi}(f)$, $\Psi_{vj}(f)$ and $\Psi_n(f)$ are broadband and exhibit slow spectral decay, when $f \in f_k \pm \delta$, $r(f)$ can be approximated as a constant value:

$$r(f) = \frac{\Psi_n(f) + \Psi_{vj}(f)H_j(f)}{\Psi_{vi}(f)} \approx r(f_k) = a_k + ib_k \tag{18}$$

Where $a_k = \Re\{r(f_k)\}$ and $b_k = \Im\{r(f_k)\}$ are slowly varying parameters, therefore:

$$\begin{aligned} |H_i(f) + r(f)|^2 &\approx |i\alpha\delta + a_k + ib_k|^2 = {a_k}^2 + (\alpha\delta + b_k)^2 \\ &= \alpha^2\delta^2 + 2\alpha b_k\delta + {a_k}^2 + {b_k}^2 \end{aligned} \tag{19}$$

Differentiating Eq. (19) with respect to δ yields:

$$\frac{\mathrm{d}}{\mathrm{d}\delta}|H_i(f) + r(f)|^2 = 2\alpha^2\delta + 2\alpha b_k, \frac{\mathrm{d}^2}{\mathrm{d}\delta^2}|H_i(f) + r(f)|^2 = 2\alpha^2 > 0 \tag{20}$$

Optics EXPRESS

Hence the stationary point is uniquely determined as:

$$\delta_k{}^* = -\frac{\mathrm{b}_k}{\alpha} \tag{21}$$

By applying a logarithmic transformation converts the magnitude spectrum of $\Psi(f)$. Around each $f_k + \delta_k^*$, the resulting signal can then be approximated as:

$$\begin{aligned}\log|\Psi(f)| &= \log|H_i(f) + r(f)| + \log|\Psi_{vi}(f)| \\ &\approx \frac{1}{2}\log(\alpha^2(f-(f_k+\delta_k{}^*))^2 + a_k{}^2) + \log|\Psi_{vi}(f-(f_k+\delta_k{}^*))| \\ &\approx \frac{1}{2}\log\left(\left(f-\left(\frac{k}{\Delta t_i}-\frac{\mathrm{b}_k}{\alpha}\right)\right)^2 + \left(\frac{a_k}{\alpha}\right)^2\right) + \log\alpha + \log|\Psi_{vi}(f_k+\delta_k{}^*)|\end{aligned} \tag{22}$$

We use the following standard transform pair:

$$\mathcal{F}^{-1}\{\log((f-f_0)^2+a^2)\} \approx -\frac{1}{|\tau|}e^{-2\pi a|\tau|}\cos(2\pi f_0\tau) + \log a^2\delta(\tau) \tag{23}$$

By applying Eq. (23) to the inverse Fourier transform converts Eq. (22) around each index k, the resulting signal can be approximated as:

$$\begin{aligned}S_k(\tau) &\approx \mathcal{F}^{-1}\left\{\frac{1}{2}\log\left(\left(f-\left(\frac{k}{\Delta t_i}-\frac{\mathrm{b}_k}{\alpha}\right)\right)^2 + \frac{a_k{}^2}{\alpha^2}\right) + \log\alpha + \log|\Psi_{vi}(f_k+\delta_k{}^*)|\right\} \\ &= -\frac{1}{2|\tau|}e^{-\frac{a_k}{\Delta t_i}|\tau|}\cos\left(2\pi\tau\left(\frac{k}{\Delta t_i}-\frac{\mathrm{b}_k}{\alpha}\right)\right) + (\log a_k + \log|\Psi_{vi}(f_k+\delta_k{}^*)|)\delta(\tau) \\ &= s_k(\tau) + c_k(\tau)\end{aligned} \tag{24}$$

where $s_k(\tau)$ denotes the oscillatory factor and c_k collects the constans.

Summing over all $k \in \mathbb{Z}$ converts Eq. (24), let $C_k(\tau)$ collect the constant contributions.

$$\begin{aligned}C_i(\tau) &= \sum_k S_k(\tau) = -\frac{1}{2|\tau|}\sum_k e^{-\frac{a_k}{\Delta t_i}|\tau|}\cos\left(2\pi\tau\left(\frac{k}{\Delta t_i}-\frac{\mathrm{b}_k}{\alpha}\right)\right) + C_k(\tau) \\ &= -\frac{1}{2|\tau|}\Re\left\{\sum_k e^{-\frac{a_k}{\Delta t_i}|\tau|}e^{-i2\pi\tau\frac{\mathrm{b}_k}{\alpha}}e^{i2\pi\tau\frac{k}{\Delta t_i}}\right\} + C_k(\tau)\end{aligned} \tag{25}$$

Using the Poisson summation formula and the sifting property of the Dirac delta [28]:

$$\begin{aligned}\sum_{k=-\infty}^{+\infty} e^{i2\pi\tau\frac{k}{\Delta t_i}} &= \Delta t_i \sum_{m=-\infty}^{+\infty}\delta(\tau - m\Delta t_i) \\ f(\tau)\delta(\tau - m\Delta t_i) &= f(m\Delta t_i)\delta(\tau - m\Delta t_i)\end{aligned} \tag{26}$$

The resulting signal of Eq. (25) can be expressed as:

$$\begin{aligned}C_i(\tau) &= -\frac{1}{2|\tau|}\Re\left\{\Delta t_i\sum_{m=-\infty}^{+\infty}\left(\sum_k e^{-|m|a_k}e^{-i|m|b_k}\right)\delta(\tau - m\Delta t_i)\right\} + C_k(\tau) \\ &= -\sum_{m\neq 0}\frac{1}{2|m|}\Re\left\{\sum_k e^{-|m|a_k}e^{-i|m|b_k}\right\}\delta(\tau - m\Delta t_i) + C_k(\tau) \\ &= \sum_{m\neq 0} A_m\delta(\tau - m|\Delta t_i|) + C_k(\tau)\end{aligned} \tag{27}$$

Optics EXPRESS

where

$$A_m = -\frac{1}{2|m|}\Re\left\{\sum_k e^{-|m|a_k}e^{-i|m|b_k}\right\} \tag{28}$$

denotes the amplitude of the impulse located at $\tau = m|\Delta t_i|$.

Based on the above derivation, the impulses at $\tau = m|\Delta t_i|$ are generated by the periodic modulation in the magnitude spectrum with a frequency period $1/|\Delta t_i|$. To ensure that this periodic structure can be properly resolved in practice, the vibration signal must provide sufficient effective bandwidth. Specifically, the bandwidth B_i should satisfy:

$$B_i \gtrsim \frac{1}{|\Delta t_i|} \tag{29}$$

By following the same derivation steps as in Eqs. (15)–(29), for $j \neq i$, the derivation for the j is identical to that for the i. The resulting signal of Eq. (8) can be approximated as:

$$\begin{aligned} C_\varphi(\tau) &= C_i(\tau) + C_j(\tau) + C_{slow}(\tau) \\ &\approx -\sum_{m\neq 0} A_m\delta(\tau - m|\Delta t_i|) - \sum_{n\neq 0} B_n\delta(\tau - n|\Delta t_j|) + C_{slow}(\tau) + C_k(\tau) \\ &= -\sum_{m\neq 0} A_m\delta(\tau - m|\Delta t_i|) - \sum_{n\neq 0} B_n\delta(\tau - n|\Delta t_j|) + C_{base}(\tau) \end{aligned} \tag{30}$$

where $C_{base}(\tau)$ denotes the baseline component of the cepstrum. It includes the terms associated with the vibration source spectrum $C_{slow}(\tau)$ and constant factors $C_k(\tau)$. The impulses $\delta(\tau - m|\Delta t_i|)$ and $\delta(\tau - n|\Delta t_j|)$ thus yield peaks at $\tau = m|\Delta t_i|$ and $\tau = n|\Delta t_j|$.

Appendix B: Derivation of the sign of the delay time

From the first cepstrum step we only know the absolute value of the true delay $|T_1|>0$. We define the following two candidate residual signals:

$$\begin{aligned} \mathbf{A1}: r_{A1}(t) &= \varphi_1(t - |T_1|) - \varphi_2(t) \\ \mathbf{B1}: r_{B1}(t) &= \varphi_2(t - |T_1|) - \varphi_1(t) \end{aligned} \tag{31}$$

For each case we compute the residual energy:

$$E_{A1} = \int |r_{A1}(t)|^2 \mathrm{d}t, E_{B1} = \int |r_{B1}(t)|^2 \mathrm{d}t \tag{32}$$

The vibration source can be aligned and cancel out only when the sign of delay T_1 is correct. In this situation the residual energy is minimized. Therefore, by identifying the smallest residual energy between E_{A1} and E_{B1}, we determine the correct sign of the delay time. The true delay T_1 can be expressed as:

$$T_1 = \mathrm{sgn}(T_1)\cdot|T_1| = \mathrm{sgn}(E_{B1} - E_{A1})\cdot|T_1| \tag{33}$$

Then we assume that the true delay of the other vibration source is T_2. From the second cepstrum step we know the absolute value of the difference of the two delays $T = |T_2 - T_1|>0$.

Optics EXPRESS

Therefore, there are two candidates for delay T_2:

$$\begin{aligned} {T_2}^+ &= T_1 + T \\ {T_2}^- &= T_1 - T \end{aligned} \tag{34}$$

For each candidate we construct the residual signals in the same manner as Eq. (34):

$$\begin{aligned} \mathbf{A2}: r_{A2}(t) &= \varphi_1(t - {T_2}^+) - \varphi_2(t) \\ \mathbf{B2}: r_{B2}(t) &= \varphi_2(t - {T_2}^+) - \varphi_1(t) \\ \mathbf{C2}: r_{C2}(t) &= \varphi_1(t - {T_2}^-) - \varphi_2(t) \\ \mathbf{D2}: r_{D2}(t) &= \varphi_2(t - {T_2}^-) - \varphi_1(t) \end{aligned} \tag{35}$$

The corresponding residual energies can be expressed as:

$$E_{A2} = \int |r_{A2}(t)|^2 \mathrm{d}t, E_{B2} = \int |r_{B2}(t)|^2 \mathrm{d}t, E_{C2} = \int |r_{C2}(t)|^2 \mathrm{d}t, E_{D2} = \int |r_{D2}(t)|^2 \mathrm{d}t \tag{36}$$

Only when the four candidate equals the true delay T_2, the vibration source about this delay can be aligned and cancel out, and the corresponding residual energy becomes minimal. Therefore, by comparing the minimum energies, we uniquely determine the true delay T_2.

$$T_2 = T_1 + \mathrm{sgn}(\min\{E_{C2}, E_{D2}\} - \min\{E_{A2}, E_{B2}\}) \cdot T \tag{37}$$

Funding. National Natural Science Foundation of China (W2532046, 62275172, U22A2088); Shenzhen Science and Technology Program (JCYJ20241202124408012, JCYJ20220818095800001); Shenzhen Science and Technology Program (Shenzhen Key Laboratory of Ultrafast Laser Micro/Nano Manufacturing) (ZDSYS20220606100405013); Scientific Instrument Developing Program of Shenzhen University (2023YQ027); Research Team Cultivation Program of Shenzhen University (2023DFT001).

Disclosures. The authors declare no conflicts of interest.

Data availability. Data underlying the results presented in this paper are not publicly available at this time but may be obtained from the authors upon reasonable request.

References

1. X. Yin and M. Wang, "Science mapping for recent research regarding urban underground infrastructure," Buildings **12**(11), 2031 (2022).
2. F. Bergman, S. Anderberg, J. Krook, *et al.*, "A critical review of the sustainability of multi-utility tunnels for colocation of subsurface infrastructure," Frontiers in Sustainable Cities **4**, 847819 (2022).
3. J. Li and S. Li, "Recent advances and applications towards intelligent operation and maintenance of urban pipeline networks," Urban Lifeline **1**(1), 2 (2023).
4. M. Wang and X. Yin, "Construction and maintenance of urban underground infrastructure with digital technologies," Automation in Construction **141**, 104464 (2022).
5. B. G. Gorshkov, K. Yüksel, A. A. Fotiadi, *et al.*, "Scientific applications of distributed acoustic sensing: State-of-the-art review and perspective," Sensors **22**(3), 1033 (2022).
6. X. Liu, B. Jin, Q. Bai, *et al.*, "Distributed fiber-optic sensors for vibration detection," Sensors **16**(8), 1164 (2016).
7. Z. Ding, C. Wang, K. Liu, *et al.*, "Distributed optical fiber sensors based on optical frequency domain reflectometry: A review," Sensors **18**(4), 1072 (2018).
8. B. Lu, B. Wu, J. Gu, *et al.*, "Distributed optical fiber hydrophone based on Φ-OTDR and its field test," Opt. Express **29**(3), 3147–3162 (2021).
9. C. Shang, C.-Q. Wu, Z.-Y. Li, *et al.*, "A new distributed measurement of birefringence vectors by P-OTDR assisted by a high speed polarization analyzer," Chin. Phys. Lett. **28**(9), 094212 (2011).
10. X. Rao, Y. Wang, M. Chen, *et al.*, "150 km single-span distributed vibration sensor based on compensated self-interference forward transmission," J. Lightwave Technol. **42**(16), 5736–5742 (2024).
11. M. Chen, X. Rao, K. Liu, *et al.*, "Distributed vibration sensing based on a forward transmission polarization-generated carrier," Sensors **24**(16), 5257 (2024).
12. J. Huang, Y. Chen, H. Peng, *et al.*, "A 150 km distributed fiber-optic disturbance location sensor with no relay based on the dual-Sagnac interferometer employing time delay estimation," Opt. Commun. **479**, 126420 (2021).
13. H. Dang, Y. Tian, H. Liu, *et al.*, "Dynamic wavelength calibration based on synchrosqueezed wavelet transform," Opt. Express **30**(26), 46722–46733 (2022).

Optics EXPRESS

14. K. Liu, X. Jin, J. Jiang, *et al.*, "Interferometer-based distributed optical fiber sensors in long-distance vibration detection: A review," IEEE Sens. J. **22**(22), 21428–21444 (2022).
15. Y. Yan, C. Guo, X. Wu, *et al.*, "Distributed vibration sensing based on forward transmission and coherent detection," arXiv (2019).
16. J. Liu, H. Li, H. Y. Noh, *et al.*, "Urban sensing using existing fiber-optic networks," Nat. Commun. **16**(1), 3091 (2025).
17. R. Zhu, X. Rao, S. Dai, *et al.*, "Deep Integration of Fiber-Optic Communication and Sensing Systems Using Forward-Transmission Distributed Vibration Sensing and on–off Keying," Sensors **24**(17), 5758 (2024).
18. J. Fang, M.-F. Huang, S. Kotrla, *et al.*, "High-sensitivity forward-transmission vibration sensing for real-world event detection in urban fiber networks," in *Optical Fiber Communication Conference* (Optica Publishing Group, 2025), paper Th4C.2.
19. G. Y. Chen, M. Chen, X. Rao, *et al.*, "Deep integration between polarimetric forward-transmission fiber-optic communication and distributed sensing systems," Sensors **24**(21), 6778 (2024).
20. X. Rao, S. Dai, M. Chen, *et al.*, "Multi-point vibration positioning method for long-distance forward transmission distributed vibration sensing," Opt. Express **32**(17), 30775–30786 (2024).
21. Z. Ye, J. Wang, C. Wang, *et al.*, "A positioning algorithm realized multilateration for distributed fiber-optic sensor," Microw. Opt. Technol. Lett. **58**(12), 2913–2917 (2016).
22. Y. Yan, F. N. Khan, B. Zhou, *et al.*, "Forward transmission based ultra-long distributed vibration sensing with wide frequency response," J. Lightwave Technol. **39**(7), 2241–2249 (2021).
23. J. Fang, Y. Li, W. Kohno, *et al.*, "Multi-event forward-transmission vibration sensing with dual-sensor adaptive beamforming," in *Optical Fiber Communications Conference (OFC)* (IEEE, 2025), paper Th3F.5.
24. Z. Pang, G. Wang, F. Wang, *et al.*, "Fiber-based distributed sensing laser interferometer enabled by mirror-image correlation method," Adv. Photonics Nexus **3**(06), 066007 (2024).
25. J. Wu, R. Zhuo, S. Wan, *et al.*, "Intrusion location technology of Sagnac distributed fiber optical sensing system based on deep learning," IEEE Sens. J. **21**(12), 13327–13334 (2021).
26. R. B. Randall, "A history of cepstrum analysis and its application to mechanical problems," Mech. Syst. Signal Process **97**, 3–19 (2017).
27. S. Qu, Z. Liu, Y. Xu, *et al.*, "Phase sensitive optical time domain reflectometry based on compressive sensing," J. Lightwave Technol. **37**(23), 5766–5772 (2019).
28. A. V. Oppenheim and R. W. Schafer, *Digital Signal Processing*, 2nd ed. (Prentice Hall, 1975), Chap. 10, pp. 513–515.